SOFT ROBOTICS
Volume 00, Number 00, 2021

DOI: 10.1089/soro.2020.0075

SoRo
Soft Robotics

Harnessing the Multistability of Kresling Origami for Reconfigurable Articulation in Soft Robotic Arms

Joshua Kaufmann, Priyanka Bhovad, and Suyi Li

Abstract

This study examines a biology-inspired approach of using reconfigurable articulation to reduce the control requirement for soft robotic arms. We construct a robotic arm by assembling Kresling origami modules that exhibit predictable bistability. By switching between their two stable states, these origami modules can behave either like a flexible joint with low bending stiffness or like a stiff link with high stiffness, without requiring any continuous power supply. In this way, the robotic arm can exhibit pseudo-linkage kinematics with lower control requirements and improved motion accuracy. A unique advantage of using origami as the robotic arm skeleton is that its bending stiffness ratio between stable states is directly related to the underlying Kresling design. Therefore, we conduct extensive parametric analyses and experimental validations to identify the optimized Kresling pattern for articulation. The results indicate that a higher angle ratio, a smaller resting length at contracted stable state, and a large number of polygon sides can offer more significant and robust bending stiffness tuning. Based on this insight, we construct a proof-of-concept, tendon-driven robotic arm consisting of three modules and show that it can exhibit the desired reconfigurable articulation behavior. Moreover, the deformations of this manipulator are consistent with kinematic model predictions, which validate the possibility of using simple controllers for such compliant robotic systems.

Keywords: articulation, Kresling origami, multistability, manipulator

Introduction

The ongoing advances in biomimicry, material science, advanced fabrication, and control theory are enabling us to build genuinely soft robotic arms (or robotic manipulators) that can collaborate with humans in unstructured and dynamic task environments.[1–5] These robotic arms are constructed with soft materials featuring low elastic moduli and high strains before failure, so that they can passively deform their bodies and conform to different objects. This flexibility makes them inherently superior to and safer than the traditional rigid-linked robotic manipulator in human–robot interactions,[6–8] thus opening up many potential applications in minimally invasive surgeries[9–12] and assistive health care.[13–15] However, the compliant and continuous nature of these soft robotic arms also imposes significant challenges for effective modeling and control.[16–20] They usually struggle to achieve a high level of precision regarding their arm configuration and movement control because their soft bodies are high-dimensional and severely underactuated. Furthermore, soft materials can exhibit complicated viscoelastic properties with substantial uncertainties. As a result, inverse kinematics and overall structural shape are difficult to predict, making control tasks such as path planning inaccurate and computationally expensive.[19] We are still far away from widely and commercially adopting soft robotics in many aspects of our modern life.

One approach to address the control challenge of soft robotic arms is to decrease their effective degrees of freedom, and nature provides terrific examples of this strategy. For example, the octopus can generate a quasi-articulated structure with its arm, similar to that of a human, to achieve precise point-to-point movement and fetch fast-moving prey within seconds.[21] The octopus achieves such arm reconfiguration by selectively stiffening sections of its muscles and leaving other sections flexible. Such reconfigurable structural articulation allows a drastically simplified control by reducing the kinematic degrees of freedom from effectively infinite to a finite

Department of Mechanical Engineering, Clemson University, Clemson, South Carolina, USA.

amount, thus granting the necessary accuracy to carry out the rapid fetching. To implement this bioinspired articulation strategy with a soft robotic arm, one must devise a method of localized stiffness tuning to create and activate discrete ''joints'' at different locations. To this end, researchers have achieved some success using jamming-based systems,[22,23] low melting point materials,[24] and shape-memory polymers.[25] However, these methods are limited due to their complexity and lack of scalability. They also require a continuous energy supply to maintain their respective changes in stiffness.[26]

To achieve the localized stiffness tuning in soft robotic arms in a scalable and energy-passive manner, we seek to analyze and exploit the mechanics of a bistable and cylindrical-shaped origami known as the Kresling (Fig. 1). Kresling origami originates from the buckling and collapsing deformation of a cylindrical shell under compression.[27] It exhibits a bistability—existence of two distant stable equilibria (or stable states)—and can fold between the two states through a coupled longitudinal and rotational motion.[28–32] Such bistability has led to many Kresling applications like deployable structures,[28,33] reconfigurable antenna,[34] cellular materials,[35,36] vibration control,[37] mechanical memory,[38,39] and robotics.[40–42] More importantly, each stable state of Kresling possesses unique mechanical properties according to its folding geometry, which enables a method of binary bending stiffness tuning. Therefore, we can construct a soft robotic arm by serially connecting Kresling cells (or modules) and create joint(s) at any desired locations by switching these cells between their stable states (Fig. 1). This approach is unique in that the localized stiffness tuning is embodied in the skeleton of the robot arm itself, and the mechanics are scalable because they are derived primarily from folding geometry.

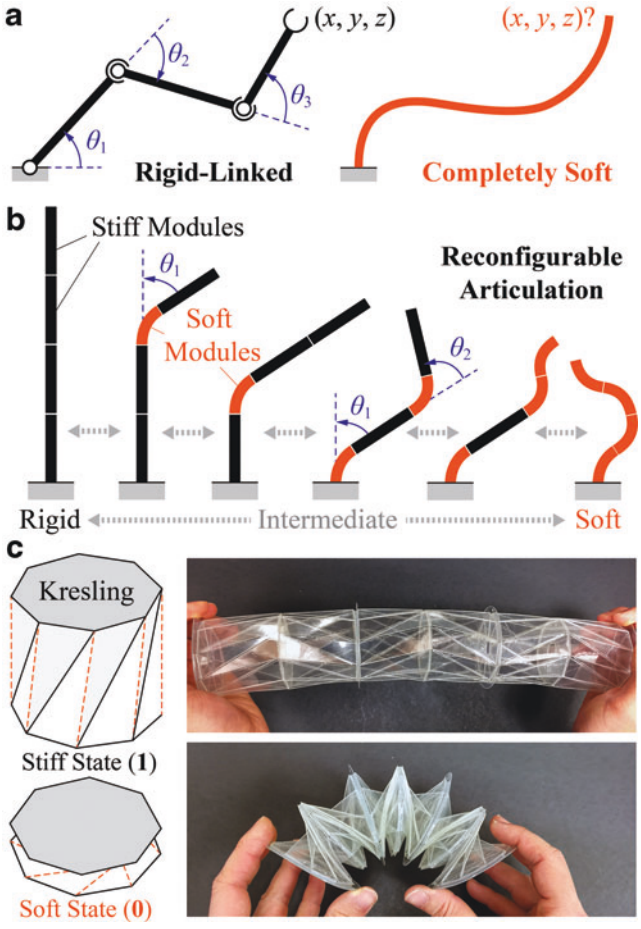

FIG. 1. An overview of the envisioned reconfigurable articulation in a continuous and compliant robotic arm. **(a)** The current paradigms of the completely rigid or completely soft robotic arm. **(b)** Different articulations of a reconfigurable arm consisting of four modules. Each module has a relatively stiff stable state and soft state so that this arm can switch from being entirely stiff (*left*) to entirely flexible (*right*), as well as to many intermediate configurations with a predictable degree-of-freedom. Notice that this conceptual robotic arm has 16 ($=2^4$) unique configurations, and this figure only shows a few representative examples. **(c)** Kresling origami can naturally show the desired switch in bending stiffness between its stable states. In this study, it will be used as the functional skeleton of the robotic arm. Color images are available online.

The objective of this study is twofold. First, we examine the correlation between Kresling origami design and the bending stiffness ratio between its two stable states. A significant and robust change in bending stiffness is the key to successful articulation in the soft robotic arm. To this end, we use a nonlinear bar-hinge model, together with experimental validation, to identify the optimized Kresling pattern design. Parametric analysis findings indicate that a higher angle ratio, a smaller resting length at the contracted stable state, and a large number of polygon sides result in a considerable change in bending stiffness. In particular, the reorientation of the triangular facets between stable states plays a crucial role.

Based on these insights, the second objective of this study is to validate the feasibility of manipulator articulation through multistability. To this end, we construct a proof-of-concept, tendon-driven manipulator consisting of three Kresling modules and show that it can exhibit the desired reconfigurable articulation behavior. Moreover, the deformation of this manipulator is consistent with the kinematic model prediction, which validates the feasibility of using simple controllers for such compliant robotic systems.

In what follows, Design and Construction of Generalized Kresling section of this article briefly reviews the design of the generalized Kresling origami, which is a variation of the classical Kresling pattern to accommodate the kinematic requirement of robotic manipulation. Bending Stiffness Tuning of Kresling Modules section details the parametric analysis and experimental testing of the bending stiffness of a Kresling origami module, as well as the robustness of the Kresling bistability against external payload. Robotic Arm Articulation section details two test results of the reconfigurable articulation behaviors of robotic arm prototypes. Finally, Conclusion section concludes this article with a summary and discussion. The results of this study will lay down the foundation for constructing a new family of hybrid soft robotics arms that are both flexible in operation and precise in motion capability.

Design and Construction of Generalized Kresling

A generalized Kresling origami cell consists of a group of triangular facets connected by two polygon end surfaces (Fig. 2). Once assembled, the Kresling cell takes a twisted polygonal prism shape. The convex creases (or mountain

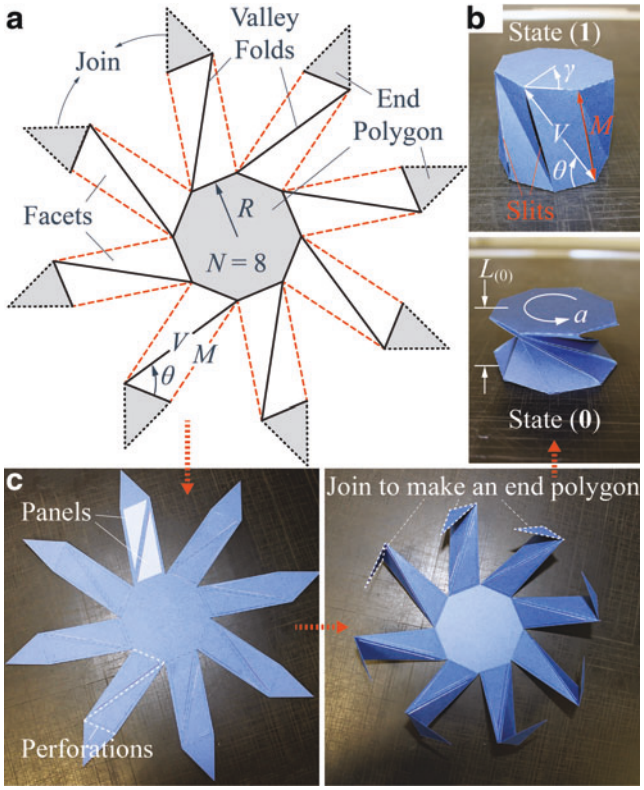

FIG. 2. Design and construction of a paper based Kresling origami cell. In this design $N = 8$, $\lambda = 0.8$, $L_{(0)} = 30$ mm, and $R = 30$ mm. **(a)** The origami crease pattern showing different design parameters. Notice that the triangular tips should be joined together to form an end polygon. **(b)** The completed Kresling cell at two different stable states. Notice that the mountain folds on the side are open slits by design. **(c)** The intermediate states of folding Kresling. Triangular panels are attached to reinforce the facets to improve overall bistability. Color images are available online.

creases) on its side are open slits by design to ensure flexibility and robustness during folding and bending.[41] A Kresling cell can settle into an extended stable state [referred to as ''state (1)'' for simplicity hereafter] or a contracted stable state [aka. ''state (0)'']. The bistability of Kresling origami originates from its nonrigid-foldable nature. That is, the triangular facets are flat and undeformed at the two stable states, but must deform during the folding transition between these two states. If these triangular facets were strictly rigid, the Kresling segment would be unable to fold.

Four independent design parameters can fully define the crease pattern of the generalized Kresling cell. They are (1) the number of polygon sides (N), (2) radius (R), (3) resting length at the contracted stable state [$L_{(0)}$], and (4) an angle ratio (λ). Here, $L_{(0)}$ is the variable that differentiates the generalized Kresling origami from conventional Kresling. The traditional Kresling has a zero length by definition at the contracted state (a property often known as ''flat-foldable''). However, a zero resting length would prevent any kinematic freedom for bending—an essential requirement for robotic arm applications. Therefore, we generalized the Kresling design with a nonzero resting length at the state (0) to provide the freedom for bending so that the Kresling cell can work like a revolute ''joint'' in the pseudo-articulated structure. The angle ratio (λ) influences the strength of the Kresling bistability. The Kresling becomes bistable when $0.5 < \lambda < 1$. Moreover, the higher the angle ratio, the stronger the bistability becomes in that one needs to apply a higher force to fold the Kresling between two stable states.[41]

Once we prescribe the aforementioned design variables, the triangular facets can be defined as

$$V = \sqrt{4R^2 \cos^2(\gamma - \lambda\gamma) + L_{(0)}^2}, \tag{1}$$

$$M = \sqrt{P^2 + V^2 - 4PR\cos(\gamma - \lambda\gamma)\cos(\lambda\gamma)}, \tag{2}$$

$$\theta = \cos^{-1}\left(\frac{P^2 + V^2 - M^2}{2PV}\right), \tag{3}$$

where γ $(= \pi/2 - \varphi)$ is the angle between the diagonal and side of the end polygon, P $(= 2R\sin\varphi)$ is the end polygon side length, and $\varphi = \pi/N$.

To calculate the resting length of the generalized Kresling origami at its extended stable state [aka. $L_{(1)}$], we first introduce α—the relative rotation angle between the top and bottom end polygon—as the independent variable that describes the folding motion. Moreover, we assume that the end polygons are rigid, and the valley creases do not change their length. In this way, facet deformation in the Kresling cell during folding can be approximated by the shortening of mountain creases, and we can calculate the current mountain crease length (m), as well as the overall Kresling cell length (l) as functions of α[41,43]:

$$l(\alpha) = \sqrt{L_{(0)}^2 + 2R^2[\cos(\alpha + 2\varphi) - \cos(\alpha_{(0)} + 2\varphi)]}, \tag{4}$$

$$m(\alpha) = \sqrt{2R^2(1 - \cos(\alpha)) + l^2}. \tag{5}$$

Based on the equations above, one can find the extended stable state (1) by solving $m(\alpha) = M$ and fully determine the external geometry of the generalized Kresling origami cell at its two different stable states.

Bending Stiffness Tuning of Kresling Modules

We use both numerical modeling and experimental testing to examine the bending stiffness tuning of Kresling modules between their two stable states, as well as the correlations between these stiffness properties and the underlying origami design.

Methods

For numerical modeling, we adopt a nonlinear bar-hinge approach that transforms the Kresling origami into a pin-jointed bar-hinge (or truss-frame) structure. This approach uses stretchable bar elements to represent the creases and adds additional torsional spring coefficients to approximate the crease folding and facet bending stiffnesses (Fig. 3a). These simplifications result in a reduced-order model capable of analyzing

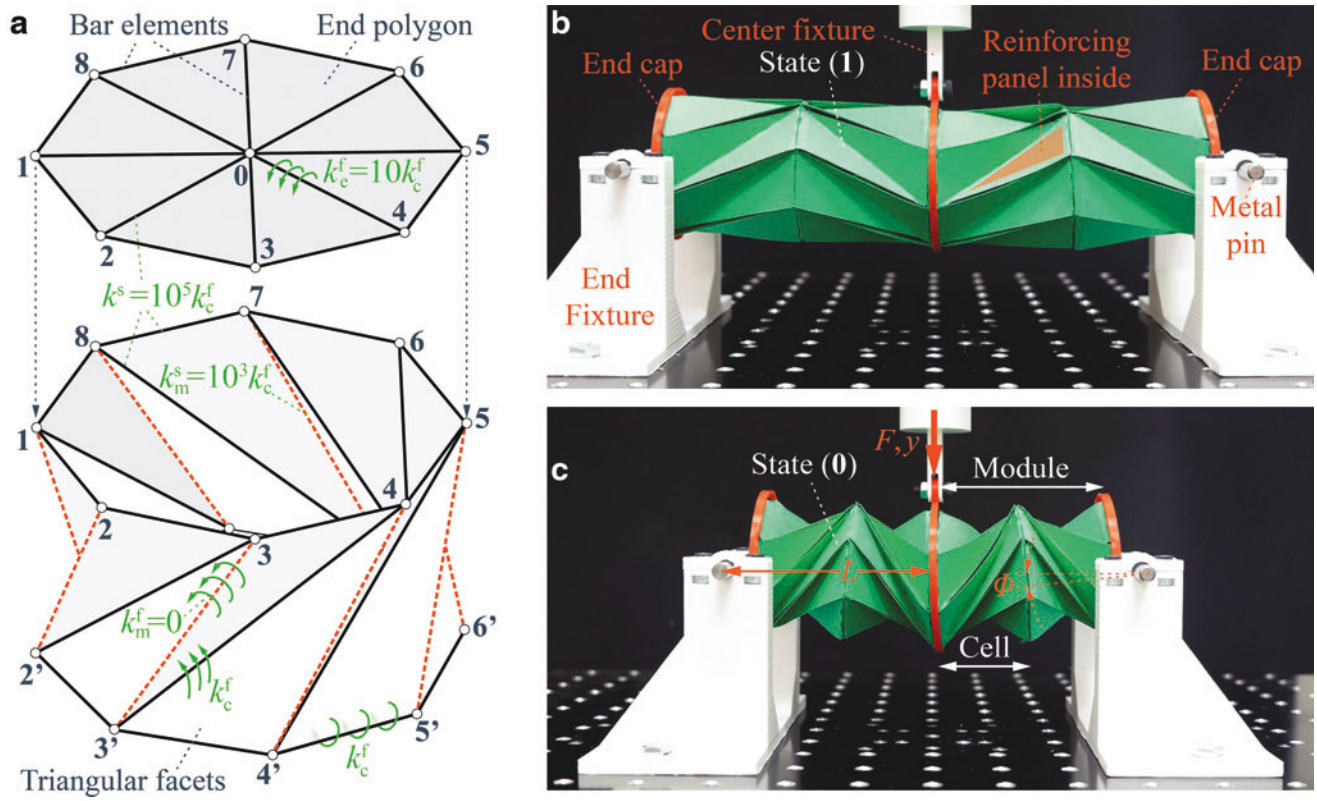

FIG. 3. The numerical and experimental methods used for testing the bending stiffness of Kresling origami. **(a)** An illustration of the nonlinear bar-hinge methods, where *solid lines* represent the stretchable bar elements, and *small circles* represent the pin-joints. The different bar rigidity and folding/bending stiffness per unit length are highlighted for clarity. **(b, c)** The three-point bending tests at two different stable states. Notice the definition of a Kresling ''module'' in **(c)**, which is an assembly of two Kresling cells of the same design but different chirality. Color images are available online.

the folding kinematics and principle deformations of Kresling origami without incurring the expensive computational cost associated with three-dimensional finite element simulations.[32] Interested readers can refer to Supplementary Appendix SA1 for the fundamentals of this bar-hinge approach and relevant literature for further details.[44,45]

The overall stiffness of the equivalent bar-hinge structure has two components. One comes from the stretching of the bar elements and the other from the folding (or bending) between adjacent triangular facets defined by these bar elements. Therefore, it is crucial to assign appropriate elastic properties to this bar-hinge system so that it can accurately represent the mechanics of the Kresling module. In this study, we assume that the axial bar rigidity (k^s) and folding/bending torsional stiffness *per unit length* (k^f) are all constant so that the Kresling nonlinearity originates from the large amplitude deformation during folding only.

There are two different types of torsional spring coefficients in this Kresling bar-hinge system. The first type is the torsional stiffness per unit length of the origami creases (k_c^f), which applies to the valley creases on the side (e.g., 2′-3 and 3′-4 in Figure 3a) and the creases between end polygons and triangular facets (e.g., 2-3 and 2′-3′). The magnitude of this stiffness is experimentally measured to be 0.047 N/radian on average (see Supplementary Appendix SA2 in for test details). The second type of torsional stiffness per unit length (k_e^f) applies to the end polygon (e.g., along 0-1 and 0-2). Its magnitude is assumed to be an order of magnitude higher than the crease torsional stiffness because it represents the polygon material bending ($k_e^f = 10k_c^f$). It is worth noting that the torsional spring coefficient of the mountain creases (e.g., 2-2′ and 3-3′) is zero due to the open slit design.

Besides the torsional spring coefficients, we assume the same axial rigidity for all bar elements in that $k^s = 10^5 k_c^f$.[44] However, one exception is the bar elements along the mountain creases on the Kresling side (e.g., 2-2′ and 3-3′). The axial rigidity of these bar elements is two orders of magnitude lower due to the slit cut design (aka. $k_m^s = 10^3 k_c^f$).

We also fabricated paper-based prototypes of the Kresling module and conducted a three-point bending test (Fig. 2b, c). To fabricate a Kresling cell, we first create the Kresling geometry in a computer-aided design program and convert it into a vectorized image file. This file is then sent to a cutting plotter (Graphtec FCX4000-50ES) that can accurately perforate the crease lines and cut the Kresling cells out of a large piece of thick paper (Daler-Rowney Canford 150 gsm). We then manually fold these cells and assemble them into Kresling modules for testing. It is worth noting that the triangular facets have reinforcement panels attached inside to increase their bending stiffness, thus increasing the bistability strength.[41]

A single Kresling cell, however, shows twisting in addition to longitudinal deformation when it folds from one stable state to the other, and this twisting is undesirable for the robotic manipulation purpose. Therefore, we construct a Kresling ''module'' by combining two kresling cells of the same design but opposite chirality (Fig. 3c). In this way,

the two end polygons of a module do not rotate with respect to each other. We secure an assembly of two identical Kresling modules to the universal testing machine (ADMET eXpert 5601) and fix them at either their extended (1) or contracted (0) stable state (Fig. 3b, c). We then apply a 5 mm downward displacement, with a rate of 0.1 mm/sec, at the center (aka. a three-point bending test). In this way, the effective bending stiffness of a Kresling module is

$$K_B = \frac{M}{\phi} = \frac{FL}{\tan^{-1}(y/L)}, \tag{6}$$

where M is the applied moment, ϕ is the rotation angle, F is the reaction force, y is the downward displacement, and L is the distance between applied force and rotation axis of the Kresling module. To characterize the performance of Kresling module, we define a ''bending stiffness ratio'' as the ratio of bending stiffness at the stiff stable state (1) to that at the soft stable state (0).

Results

Figure 4a summarizes the external moment-bending angle relationships of four Kresling module assemblies based on different crease designs. The results indicate that these origami modules can show a significant change in bending stiffness as they switch from one stable state to the other. Moreover, this change in bending stiffness is directly related to the underlying origami design. Overall, the bar-hinge model predictions correlate with the experimental results well. However, some discrepancies exist at the beginning stage of these tests. Compared to the model predictions, the experiment results show a stronger nonlinearity when the external load is small. This discrepancy probably originates from the fact that the Kresling module prototypes have to be compressed slightly before testing so that their initial length equals to the theoretically predicted resting length at the two stable states [aka. $L \approx L_{(0)}$ or $L_{(1)}$]. This small compression generates some initial stress in the structure. Regardless, the Kresling test samples show a close-to-linear behavior as the bending angle θ increases,

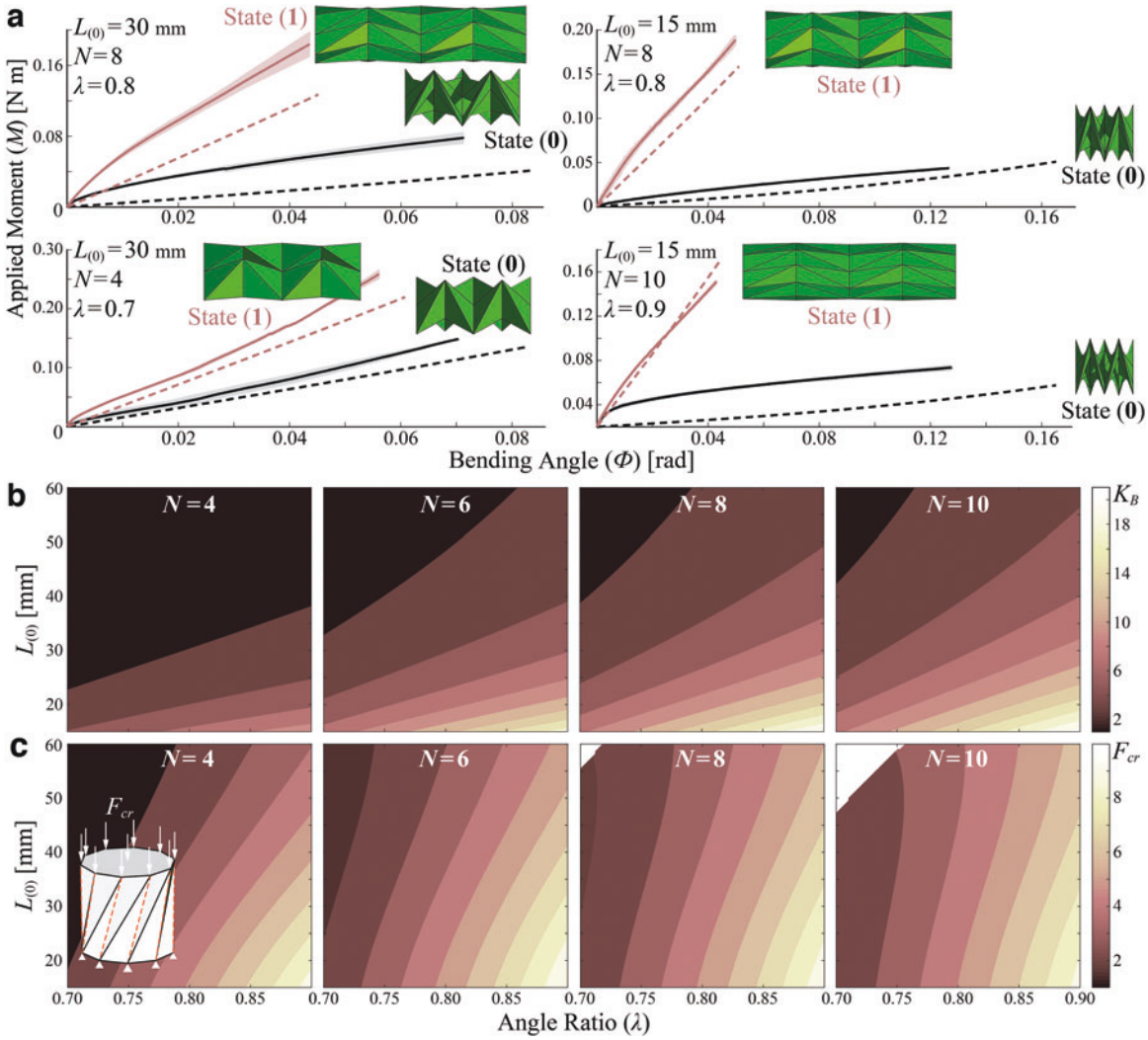

FIG. 4. Bending stiffness change between the two stable states of Kresling modules with different designs. **(a)** Experiment results of the three-point bending tests (*solid lines*) and the corresponding numerical predictions (*dashed lines*). The shaded bands are the standard deviation of three loading cycles. **(b, c)** Parametric analysis results of the bending stiffness ratio and axial snap-through force (in N), respectively. Color images are available online.

Table 1. Summary of the Three-Point Bending Test Results on Four Different Kresling Module Samples

Design	*Test*	K_B *at (1)*	K_B *at (0)*	K_B *ratio*
$N=8$, $\lambda=0.8$, $L_{(0)}=30$ mm	Experiment	3.50 ± 0.29	0.80 ± 0.07	4.9
	Bar-Hinge	2.79	0.48	5.8
$N=8$, $\lambda=0.8$, $L_{(0)}=15$ mm	Experiment	3.59 ± 0.17	0.29 ± 0.01	12.3
	Bar-Hinge	3.08	0.27	11.4
$N=4$, $\lambda=0.7$, $L_{(0)}=30$ mm	Experiment	4.31 ± 0.09	2.20 ± 0.19	2.0
	Bar-Hinge	3.59	1.61	2.2
$N=10$, $\lambda=0.9$, $L_{(0)}=15$ mm	Experiment	2.88 ± 0.03	0.25 ± 0.02	11.5
	Bar-Hinge	3.35	0.20	16.8

The unit of bending stiffness K_B is [N m/rad].

and the analytical and experimental results agree well with each other in terms of the slope of these moment-angle curves (Table 1).

Based on the experimentally validated model, we conduct a parametric analysis to obtain a comprehensive understanding of how we can tune the bending stiffness by tailoring the underlying Kresling design (Fig. 4b). In this analysis, we keep the Kresling module radius R as a constant at 30 mm because it is usually determined by specific application requirements. We vary the magnitude of the other three independent design parameters such that the polygon side number N is 4, 6, 8, or 10, the angle ratio λ is between 0.7 and 0.9, and the resting length at the contracted stable state $L_{(0)}$ is between 15 and 60 mm. These parameter ranges are chosen carefully according to the fabrication constraints. The numerical simulation results conclude that, regardless of the number of polygon sides, maximizing the angle ratio λ or minimizing the contracted length $L_{(0)}$ can lead to a higher bending stiffness ratio. In other words, if the Kresling design possesses stronger bistability and is closer to the traditional design [aka. with zero $L_{(0)}$], it will have a higher bending stiffness ratio. Increasing the base polygon sides (N) can also increase the bending stiffness ratio. However, this benefit becomes marginal when N becomes bigger than 8.

Careful inspection of the Kresling origami geometry can reveal the physical principles that underpin this stiffness change. At the extended stable state (1), the triangular facets in the Kresling origami align close to parallel to the longitudinal axis of the cylindrical-shaped module, so the overall bending stiffness is relatively high and dominated by the facet stretching. However, at the contracted state (0), the triangular facets are orientated close to perpendicular to the longitudinal axis, so the bending stiffness is low and dictated by the crease folding. To validate this causality, we define a ''facet angle ratio'' as the ratio of the dihedral angles (angle between the triangular facet and base polygon) at state (1) to the dihedral angle at state (0). Figure 5 indicates that a higher facet angle ratio directly creates a higher bending stiffness ratio.

Finally, it is also essential that the stiffness tuning of the Kresling module is robust against external disturbances. That is, once the Kresling module settles into the targeted stable state, it should remain in this state so that external forces (e.g., from the payloads) will not create any unintentional switch. To evaluate this robustness, we use the bar-hinge model to calculate the axial force required to switch the Kresling model from the extended state to the contracted state (Fig. 4c; it is worth noting that pure bending would not create any switch between stable states). Generally speaking, the parametric analysis shows that the Kresling designs with a higher bending stiffness ratio also require a large axial force to be compressed from state (1) to (0), thus showing a more robust bistability.

In contrast, the bar-hinge model predicts that the axial force required to extend the Kresling module from the state (0) to (1) is typically smaller than the opposite compression switch. To further assess the Kresling bistability's robustness, we experimentally test robotic arm prototypes by assembling three identical and paper-based Kresling modules [or 6 Kresling cells of alternating chirality with $N=8$, $\lambda=0.8$, and $L_{(0)}=15$]. We hang these prototypes vertically and apply increasing weight at its free end until any undesirable stable state switch occurs (Fig. 6). With three Kresling modules, the robotic arm can settle into 8 ($=2^3$) different configurations. For clarity, we label these configurations by (ijk) where i, j, and k can take the value of either 0 or 1, representing the current stable state of three Kresling modules from the robotic arm base to the tip, respectively. The axial deformation of the robotic arm is directly related to these stable state configurations. The arm deforms more if more Kresling modules are in the relatively compliant state (0), especially if the module at the base is at state (0). In contrast, if the base module is at the relatively stiff state (1), the robotic arm deforms significantly less in the axial direction and can carry close to twice its body weight (32 g) before any modules switch from the state (0) to (1). These results are conservative because if one uses plastic materials to make

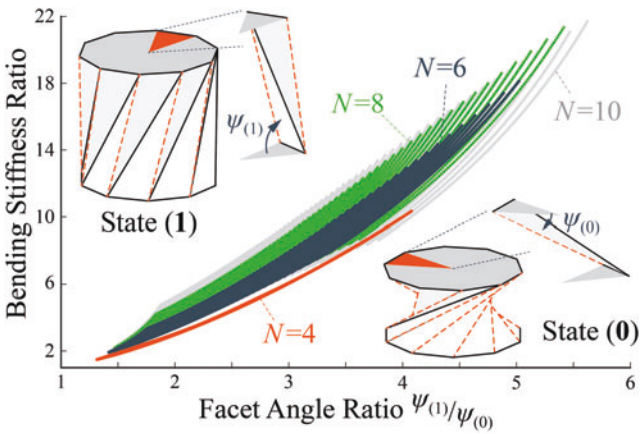

FIG. 5. The correlation between the facet angle ratio and bending stiffness ratio. Here, each point represents a unique Kresling origami design used in the parametric analyses in Figure 4. Color images are available online.

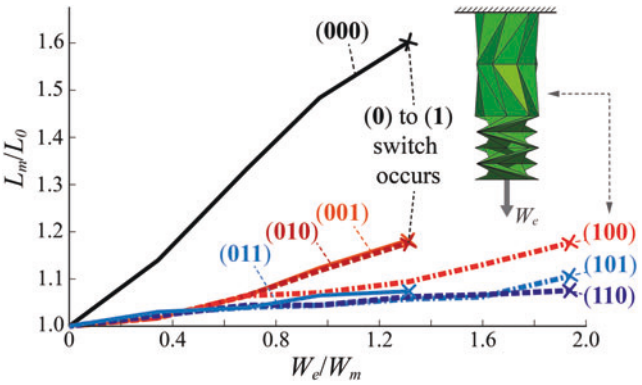

FIG. 6. Testing the Kresling bistability's robustness in tension: Here, the horizontal axis is the ratio of applied weight (aka. axial payload) over the robotic arm's weight ($W_m = 32$ gram based on the paper-based prototype), the vertical axis is the axial stretch (measured by processing the images of deformed robotic arm). If the Kresling module at the base settles at state (0), the prototype can carry ~ 1.3 times its weight before any modules switch from the state (0) to (1). If the base module is at state (1), the robotic arm can carry about twice its weight before any switch occurs. Color images are available online.

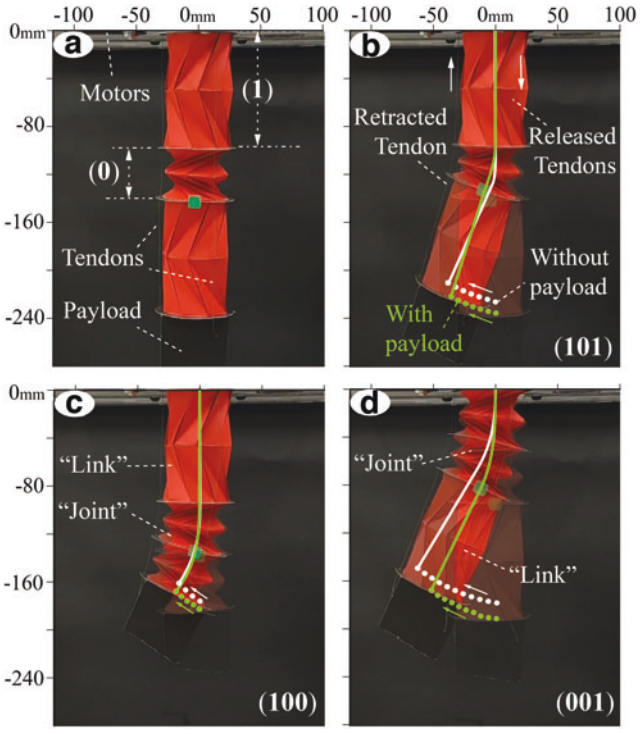

FIG. 7. Validation test of reconfigurable articulation with or without payload. **(a)** Test setup showing the robotic arm prototype configured at (101) with an end payload that weighs the same as the robotic arm itself (32 g). **(b–d)** Composite images showing robotic arm deformation under tendon actuation (Notice that the test images without payload are not shown here). The *dotted lines* show robotic arm tip displacements measured from video footage, and the *solid lines* show estimated arm shapes at the end of each test. The articulation behavior is evident regardless of the payload. Color images are available online.

Kresling origami and adds the motor-driven tendons (detailed in the next section), the manipulator's axial load capacity will further increase.

Robotic Arm Articulation

To validate the concept of reconfigurable articulation in the Kresling robotic arm, we conduct two different tests. The first test uses the same paper-based robotic arm as in the previous section's axial payload test, and the purpose of this test is to compare the articulation performance with or without the payload. The second test uses a more robust,

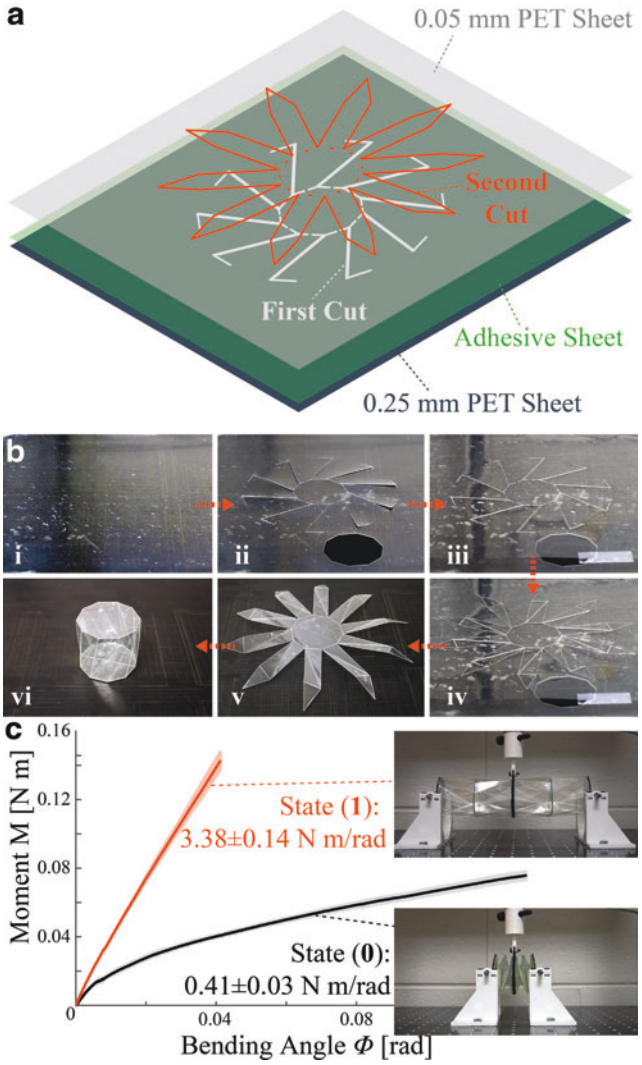

FIG. 8. Fabrication of the PET plastic-based Kresling cell for constructing the proof-of-concept robotic manipulator. **(a)** The layered construction method involves two plastic sheets, one adhesive sheet for bonding, and two different cuts. **(b)** The fabrication sequence, from *top-left* and *clockwise*, **(i)**: bond the 0.25 mm PET sheet and adhesive sheet and secure them on the cutting plotter; **(ii)**: perform the first cut, notice that an end polygon piece is also cut out; **(iii)**: attach the 0.05 mm PET sheet; **(iv)**: perform the second cut; **(v)**: remove the cut Kresling pattern from the cutting plotter; **(vi)**: manually fold the Kresling and attach it to the end polygon piece. **(c)** The three-point bending test results. PET, polyethylene terephthalate. Color images are available online.

layered polymer sheet construction for the robotic arm. The polymer Kresling modules use a different design based on the result in Figure 4 [$N = 10$, $\lambda = 0.9$, and $L_{(0)} = 15$ mm], and this test's purpose is to assess the feasibility of using simple kinematics-based model to predict the articulate arm deformation. It is worth emphasizing that since the folding geometry dictates the correlation between Kresling design and its nonlinear mechanics, insights from this study apply regardless of the materials selected.

Paper Kresling test with payload

We use three evenly spaced, motor-driven tendons routed through the Kresling robotic arm as the driving mechanism (Fig. 7). Obviously, out of the eight possible stable state configurations, the (111) configuration is immobile since all Kresling modules are in the stiffer stable state (1), and the (000) configuration is entirely soft, just like the more conventional soft manipulators. In this study, we manually set the Kresling robotic arm into the desired articulation configuration, and the methods of automatic reconfiguration will be a subject of a follow-up study.

After configuring the robotic arm, we attach a payload—which weights the same as the robotic arm itself—to its free end. It is worth highlighting that the tendons are loose during this step. The motors are then activated to retract one tendon and release the other two, creating a bending motion that simulates the object relocation task. The robotic arm deformations shown in Figure 7 validate the feasibility of reconfigurable articulation. That is, Kresling modules settled at the stable state (0) act as joints, while those at state (1) act as links. Moreover, the presence of the end payload does not negate the articulation characteristics. The tip displacement of the robotic arm, measured from the video footage using MATLAB image processing program, is similar between the scenarios with and without payload, indicating the robustness of reconfigurable articulation using Kresling bistability.

Polymer Kresling test for kinematics assessment

In the plastic-based Kresling, a layer of 0.25 mm thick polyethylene terephthalate (PET) sheet serves as the base material for the facets, and an additional layer of 0.05 mm thick PET sheet is used for the flexible creases. F9460PC adhesive transfer tape bonds these polymer sheets seamlessly (see Fig. 8 for fabrication details). A three-point bending test shows that the plastic Kresling module can exhibit a bending stiffness ratio of 8.24 between its two stable states.

Figure 9 summarizes the robotic arm deformation with different configurations. It is worth noting that, unlike the previous paper-based manipulator test where the tendons are loose before testing, we apply small pretension to the tendon in this test so that kresling modules' initial lengths are the same as the bar-hinge model prediction. This setup increases the kinematics modeling accuracy as we detail below; it also has an additional benefit of further improving the payload capacity. To illustrate the feasibility of using simple controllers for the articulated Kresling robotic arm, we attach

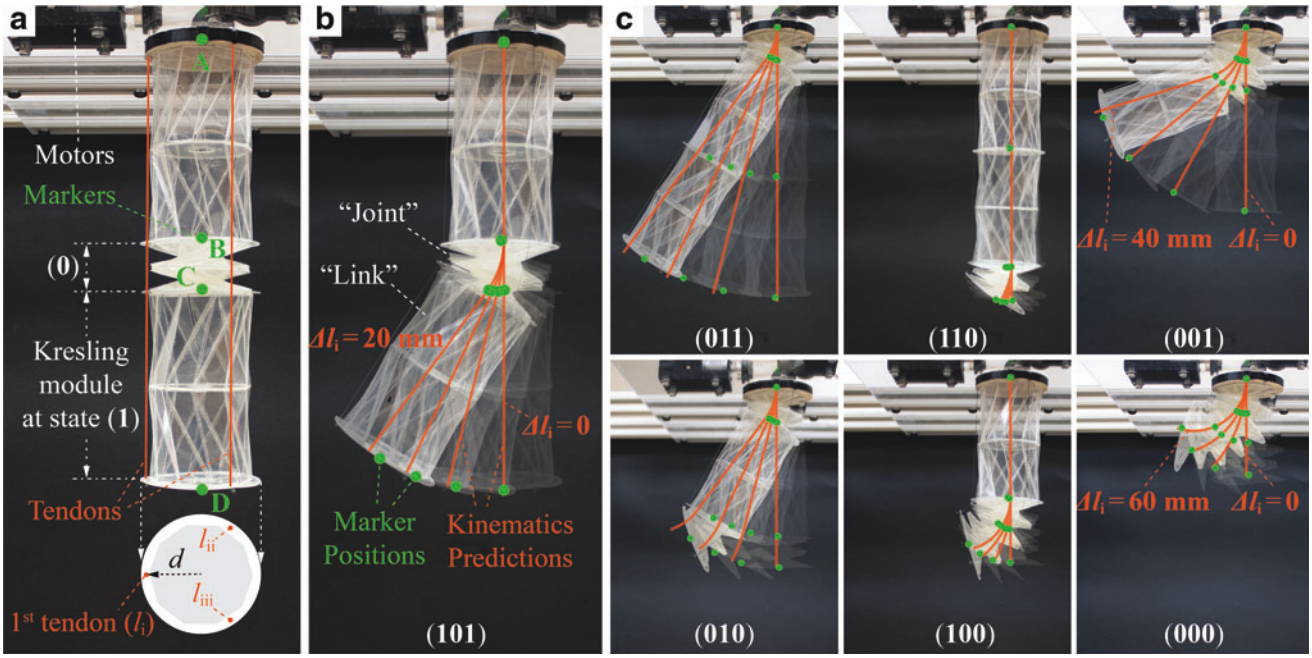

FIG. 9. Assessing the kinematics of Kresling robotic arm with reconfigurable articulation. **(a)** Test setup that shows the arm with three identical Kresling modules. The three motor-driven, evenly-spaced tendons i, ii, and iii are highlighted. We also attached *green-colored* markers A, B, C, and D at the end points of each Kresling module to facilitate measurement. **(b)** A composite image that shows the robotic arm deformation—with the (101) configuration—at different tendon actuation levels. The predicted arm deformations based on the kinematic model are plotted directly on top of the composite image as *solid lines*, which show good agreement with the *green marker positions*. **(c)** Similar composite images showing the robotic arm deformations and corresponding kinematic predictions at all other stable configurations. In these composite images, the tendon actuation $\Delta l_i = 0$, $8n_{(0)}$, $14n_{(0)}$, and $20n_{(0)}$mm, respectively, where $n_{(0)}$ is the number of Kresling modules at state (0) corresponding to the current articulation configuration. For example, $n_{(0)} = 1$ for (101), $n_{(0)} = 2$ for (001), and $n_{(0)} = 3$ for (000). Color images are available online.

green-colored markers at the end points of each Kresling module, take high resolution images of the robotic arm at different tendon actuation inputs, use image processing software to accurately measure the arm deformation by tracking the position of markers, and finally compare these measurements to analytical predictions based on a kinematic model. In Figure 9b, c, the kinematic predictions are plotted directly on top of the corresponding robotic arm images for comparison.

The kinematic model in this study adopts the Denavit–Hartenberg convention, which represents the transformation of coordinates from the reference frame attached to one Kresling module to another.[46] By defining four different reference frames at the four end points of Kresling modules (aka. *A*, *B*, *C*, and *D* in Fig. 9b), we can describe the transformation from a reference frame *A* to frame *B* as:

$$\mathbf{H}_B^A = \begin{bmatrix} \mathbf{R}_B^A & \mathbf{o}_B^A \\ 0 & 1 \end{bmatrix}, \tag{7}$$

where $\mathbf{R}_B^A$ is a 3×3 matrix representing the orientation (rotational) transformation from frame A to frame B, and o_B^A is a 3×1 column vector representing the translation from the origin of frame A to frame B (both $\mathbf{R}_B^A$ and $\mathbf{o}_B^A$ are formulated with respect to frame A). A series of such transformations can be performed to describe the total configuration of the robotic arm shown by

$$\mathbf{H}_D^A = \mathbf{H}_B^A \mathbf{H}_C^B \mathbf{H}_D^C, \tag{8}$$

where the final result is a matrix describing the orientation and position of reference frame D with respect to frame A.

For Kresling modules at state (0), we use the Jones kinematic model that describes the shape of these soft modules as a simple arc with constant curvature.[47,48] Thus, their corresponding transformation matrix is:

$$\mathbf{H}_{(0)} = \begin{bmatrix} \cos\phi & -\sin\phi\cos\theta & \sin\phi\sin\theta & \kappa^{-1}(\sin\phi(1-\cos\theta)) \\ \sin\phi & \cos\phi\cos\theta & -\cos\phi\sin\theta & -\kappa^{-1}(\cos\phi(1-\cos\theta)) \\ 0 & \sin\theta & \cos\theta & \kappa^{-1}\sin\theta \\ 0 & 0 & 0 & 1 \end{bmatrix}, \tag{9}$$

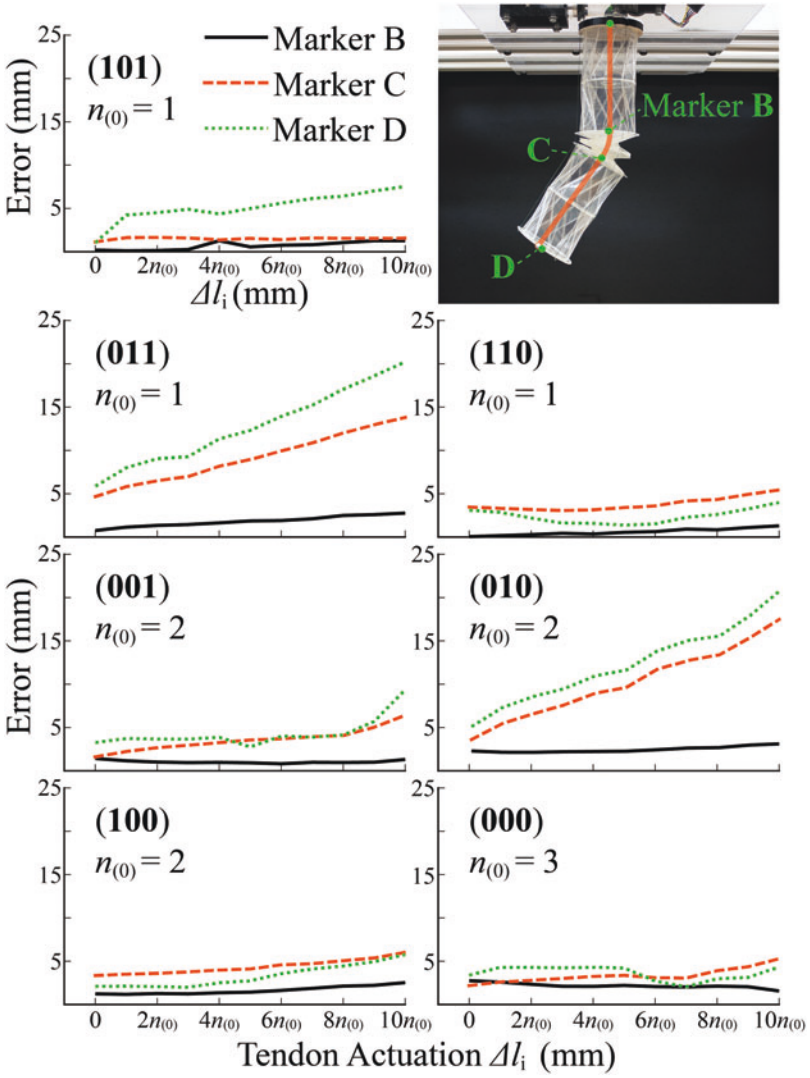

FIG. 10. The differences between experimentally measured positions of Markers B, C, and D and the corresponding kinematic model prediction. Color images are available online.

where

$$\phi = \tan^{-1}\left(\frac{\sqrt{3}}{3}\frac{l_{ii}+l_{iii}-2l_i}{l_{ii}-l_{iii}}\right), \quad (10)$$

$$\theta = 2N\ \sin^{-1}\left[\frac{\left(l_i^2+l_{ii}^2+l_{iii}^2-l_il_{ii}-l_{ii}l_{iii}-l_il_{iii}\right)^{1/2}}{3Nd}\right], \quad (11)$$

$$\kappa = K2\frac{\left(l_i^2+l_{ii}^2+l_{iii}^2-l_il_{ii}-l_{ii}l_{iii}-l_il_{iii}\right)^{1/2}}{d(l_i+l_{ii}+l_{iii})}. \quad (12)$$

Here, l_i, l_{ii}, and l_{iii} are the lengths of three driving tendons in this module, $N=1$, and d ($=32$ mm) is the distance between tendon and the longitudinal axis of Kresling module. In the tests shown in Figure 9b and c, we use the motors to pull tendon i and release tendon ii and iii simultaneously so that $\Delta l_{ii} = \Delta l_{iii} = -0.5\Delta l_i$.

For Kresling modules at state (1), we simply assume that they are straight links so that their corresponding transformation matrix is:

$$\mathbf{H}_{(1)} = \begin{bmatrix} 1 & 0 & 0 & 0 \\ 0 & 1 & 0 & 0 \\ 0 & 0 & 1 & L_{(1)} \\ 0 & 0 & 0 & 1 \end{bmatrix}, \quad (13)$$

where $L_{(1)}$ ($=111.6$mm) is the resting length of the Kresling module at the stable state (1).

Overall, the robotic arm deformations agree well with the kinematic predictions at different tendon actuation levels. Figure 10 further summarizes the differences between the experimentally measured marker positions and the corresponding predictions based on the kinematic model. For most of the stable configurations, these differences are smaller than 5 mm, which is small compared to the overall length of the robotic arm (ranging from $\sim$50 to 270 mm depending on the articulation setup). These discrepancies probably originate from fabrication imperfections, gravity, as well as other small and complex Kresling deformations due to its compliant nature. In contrast, the position errors of Markers C and D are more significant at the (011) and (010) configurations as the robotic arm is displaced further. In these two configurations, the Kresling module at the base behaves like a joint, which is immediately followed by a link-like module. As a result, the error from the base joint amplifies and accumulates further down the chain.

Regardless, the two articulation test results validate the linkage-like behavior, which can be modeled accurately with a kinematics model. Therefore, one could apply ''off-the-shelf'' feedback controllers typically used for rigid-linked robotics for the compliant Kresling robotic arm. The results also pave the way for future integration of active materials (e.g., shape memory alloy and polymers) to achieve stable state configuration autonomously. These results also lead to an interesting topic for future study: understanding how to configure the articulation of the Kresling arm to accommodate different robotic manipulation requirements (e.g., the object's shape and weight, original and targeted locations).

Conclusion

This study proposes to exploit the bistability of Kresling origami to enable localized bending stiffness tuning and reconfigurable articulation of a modular robotic arm. By strategically switching the Kresling modules between the stiff, link-like stable state (1) and soft, joint-like stable state (0), one can significantly reduce the effective degrees of freedom of a compliant manipulator to both simplify the control requirements and increase motion precision. Through both analytical studies using a nonlinear bar-hinge method and experimental validations using a customized three-point bending method, we uncover the correlations between the magnitude of bending stiffness change and the underlying crease pattern design of the Kresling module. Generally speaking, the Kresling modules with more polygon sides, lower resting length at contracted stable state, and higher angle ratio can offer a more significant and robust change in bending stiffness between their two stable states. However, the module length at stable state (0) needs to be chosen carefully to ensure sufficient kinematic freedom for bending. In experiments, the paper-based Kirigami modules achieve an order of magnitude change in bending stiffness by simply switching between two stable states, without the need for a continuous power supply to maintain this stiffness change.

We construct a tendon-driven, proof-of-concept robotic arm prototype by assembling three identical Kresling modules. This robotic arm successfully validates the concept of reconfigurable articulation by exhibiting linkage-like deformations at different stable configurations. Moreover, the magnitudes of these deformations agree well with analytical predictions according to a kinematic model. Therefore, the results of this study lay down the foundation for a reconfigurable robotic arm that can adapt to different manipulation task requirements with a significantly reduced control effort.

Author Disclosure Statement

No competing financial interests exist.

Funding Information

J.K., P.B., and S.L. acknowledge the support from Clemson University (via startup fund and Dean's Faculty Fellow Award) and the National Science Foundation (CMMI: 1751449 CAREER and 1933124).

Supplementary Material

Supplementary Appendix SAP1
Supplementary Appendix SAP2

References

1. Trivedi D, Rahn CD, Kier WM, et al. Soft robotics: biological inspiration, state of the art, and future research. Appl Bionics Biomech 2008;5:99–117.
2. Kim S, Laschi C, Trimmer B. Soft robotics: a bioinspired evolution in robotics. Trends Biotechnol 2013;31:287–294.
3. Majidi C. Soft robotics: a perspective-current trends and prospects for the future. Soft Robot 2014;1:5–11.
4. Laschi C, Mazzolai B, Cianchetti M. Soft robotics: technologies and systems pushing the boundaries of robot abilities. Sci Robot 2016;1:eaah3690.

5. Whitesides GM. Angewandte Chemie International Edition. Soft Robot 2018;57:4258–4273.
6. Sanan S, Ornstein MH, Atkeson CG. Physical human interaction for an inflatable manipulator. In: 2011 Annual International Conference of the IEEE Engineering in Medicine and Biology Society, IEEE, Boston, USA, 2011, pp. 7401–7404.
7. Runge G, Preller T, Zellmer S, et al. SpineMan: design of a soft robotic spine-like manipulator for safe human-robot interaction. In: 2015 IEEE/RSJ International Conference on Intelligent Robots and Systems (IROS), IEEE, Hamburg, Germany, 2015, pp. 1103–1110.
8. Stilli A, Wurdemann HA, Althoefer K. A novel concept for safe, stiffness-controllable robot links. Soft Robot 2017;4: 16–22.
9. Burgner-Kars J, Rucker DC, Choset H. Continuum robots for medical applications: a Survey. IEEE Trans Robot 2015; 1:1261–1280.
10. Runciman M, Darzi A, Mylonas GP. Soft robotics in minimally invasive surgery. Soft Robot 2019;6:423–443.
11. Ranzani T, Gerboni G, Cianchetti M, et al. A bioinspired soft manipulator for minimally invasive surgery. Bioinspirat Biomimet 2015;10:035008.
12. Cianchetti M, Ranzani T, Gerboni G, et al. Soft robotics technologies to address shortcomings in today's minimally invasive surgery: the STIFF-FLOP approach. Soft Robot 2014;1:122–131.
13. Polygerinos P, Wang Z, Galloway KC, et al. Soft robotic glove for combined assistance and at-home rehabilitation. Robot Autonom Syst 2015;73:135–143.
14. Connolly F, Walsh CJ, Bertoldi K. Automatic design of fiber-reinforced soft actuators for trajectory matching. Proc Natl Acad Sci USA 2017;114:51–56.
15. In H, Kang BB, Sin M, et al. Exo-Glove: a wearable robot for the hand with a soft tendon routing system. IEEE Robot Automat Magaz 2015;22:97–105.
16. Camarillo DB, Milne CF, Carlson CR, et al. Mechanics modeling of tendon-driven continuum manipulators. IEEE Trans Robot 2008;24:1262–1273.
17. Trivedi D, Lotfi A, Rahn CD. Geometrically exact models for soft robotic manipulators. IEEE Trans Robot 2008;24: 773–780.
18. Renda F, Giorelli M, Calisti M, et al. Dynamic model of a multibending soft robot arm driven by cables. IEEE Trans Robot 2014;30:1109–1122.
19. Thuruthel TG, Ansari Y, Falotico E, et al. Control strategies for soft robotic manipulators: a survey. Soft Robot 2018;5:149–163.
20. Webster RJ, Jones BA. Design and kinematic modeling of constant curvature continuum robots: a review. Int J Robot Res 2010;29:1661–1683.
21. Sumbre G, Fiorito G, Flash T, et al. Octopuses use a human-like strategy to control precise point-to-point arm movements. Current Biol 2006;16:767–772.
22. Kim Y-J, Cheng S, Kim S, et al. A novel layer jamming mechanism with tunable stiffness capability for minimally invasive surgery. IEEE Trans Robot 2013;29:1031–1042.
23. Cianchetti M, Ranzani T, Gerboni G, et al. STIFF-FLOP surgical manipulator: Mechanical design and experimental characterization of the single module. In: 2013 IEEE/RSJ International Conference on Intelligent Robots and Systems, IEEE, 2013, pp. 3576–3581.
24. Cheng N, Ishigami G, Hawthorne S, et al. Design and analysis of a soft mobile robot composed of multiple thermally activated joints driven by a single actuator. In: 2010 IEEE International Conference on Robotics and Automation, IEEE, 2010, pp. 5207–5212.
25. Firouzeh A, Mirrazavi Salehian SS, Billard A, et al. An under actuated robotic arm with adjustable stiffness shape memory polymer joints. In: 2015 IEEE International Conference on Robotics and Automation (ICRA), IEEE, 2015, pp. 2536–2543.
26. Manti M, Cacucciolo V, Cianchetti M. Stiffening in soft robotics: a review of the state of the art. IEEE Robot Automat Magaz 2016;23:93–106.
27. Hunt GW, Ario I. Twist buckling and the foldable cylinder: an exercise in origami. Int J Nonlinear Mech 2005;40:833–843.
28. Cai J, Deng X, Ya Z, et al. Bistable behavior of the cylindrical origami structure with Kresling pattern. J Mech Des 2015;137:061406.
29. Masana R, Daqaq MF. Equilibria and bifurcations of a foldable paper-based spring inspired by Kresling-pattern origami. Phys Rev E 2019;100:063001.
30. Reid A, Lechenault F, Rica S, et al. Geometry and design of origami bellows with tunable response. Phys Rev E 2017; 95:013002.
31. Fang H, Chang T-S, Wang K W. Magneto-origami structures: engineering multi-stability and dynamics via magnetic-elastic coupling. Smart Mater Struct 2020;29:015026.
32. Li S, Fang H, Sadeghi S, et al. Architected origami materials: how folding creates sophisticated mechanical properties. Adv Mater 2019;31:1805282.
33. Kidambi N, Wang KW. Dynamics of Kresling origami deployment. Phys Rev E 2020;101:063003.
34. Liu X, Yao S, Georgakopoulos SV. Mode reconfigurable bistable spiral antenna based on kresling origami. In: 2017 IEEE International Symposium on Antennas and Propagation & USNC/URSI National Radio Science Meeting, 2017, pp. 413–414.
35. Nayakanti N, Tawfick SH, Hart JA. Twist-coupled Kirigami cells and mechanisms. Extreme Mech Lett 2018;21: 17–24.
36. Tao R, Ji L, Li Y, et al. 4D printed origami metamaterials with tunable compression twist behavior and stress-strain curves. Comp B Eng 2020;201:108344.
37. Ishida S, Uchida H, Shimosaka H, et al. Design and numerical analysis of vibration isolators with quasi-zero-stiffness characteristics using bistable foldable structures. J Vibrat Acoust 2017;139:031015.
38. Yasuda H, Tachi T, Lee M, et al. Origami-based tunable truss structures for non-volatile mechanical memory operation, Nat Commun 2017;8:962.
39. Masana R, Khazaaleh S, Alhussein H, et al. An origami-inspired dynamically actuated binary switch. Appl Phys Lett 2020;117:081901.
40. Pagano A, Yan T, Chien B, et al. A crawling robot driven by multi-stable origami. Smart Mater Struct 2017;26:094007.
41. Bhovad P, Kaufmann J, Li S. Peristaltic locomotion without digital controllers: exploiting multi-stability in origami to coordinate robotic motion. Extreme Mech Lett 2019;32: 100552.
42. Novelino LS, Ze Q, Wu S, et al. Untethered control of functional origami microrobots with distributed actuation. Proc Natl Acad Sci USA 2020;117:24096–24101.

43. Bhovad P, Li S. Using multi-stable origami mechanism for peristaltic gait generation: a case study. In: Proceedings of ASME IDETC/CIE, ASME, Quebec City, Canada, 2018, p. V05BT07A061.
44. Liu K, Paulino GH. Nonlinear mechanics of non-rigid origami: an efficient computational approach. Proc R Soc A Math Phys Eng Sci 2017;473:20170348.
45. Liu K, Tachi T, Paulino GH. Invariant and smooth limit of discrete geometry folded from bistable origami leading to multistable metasurfaces. Nat Commun 2019;10:4238.
46. Spong MW, Hutchinson S, Vidyasagar M. Robot Modeling and Control. John Wiley & Sons, Inc., New York, NY, 2006.
47. Jones BA, Walker ID. Kinematics for multisection continuum robots. IEEE Trans Robot 2006;22:43–55.
48. Chawla A, Frazelle C, Walker I. A comparison of constant curvature forward kinematics for multisection continuum manipulators. In: Proceedings—2nd IEEE International Conference on Robotic Computing, IRC 2018, 2018.

Address correspondence to:
Suyi Li
Department of Mechanical Engineering
Clemson University
216 South Palmetto Boulevard
Clemson, SC 29634
USA

E-mail: suyil@clemson.edu